JOURNAL OF COMPUTATIONAL PHYSICS 70, 330–354 (1987)

Semi-implicit Magnetohydrodynamic Calculations

D. D. SCHNACK, D. C. BARNES, Z. MIKIC

Applied Plasma Physics and Technology Division,
Science Applications International Corporation,
La Jolla, California 92038

DOUGLAS S. HARNED

Courant Institute of Mathematical Sciences, New York University,
New York, New York 10012

AND

E. J. CARAMANA

Los Alamos National Laboratory, Los Alamos, New Mexico 87545

Received April 11, 1986; revised September 12, 1986

A semi-implicit algorithm for the solution of the nonlinear, three-dimensional, resistive MHD equations in cylindrical geometry is presented. The specific model assumes uniform density and pressure, although this is not a restriction of the method. The spatial approximation employs finite differences in the radial coordinate, and the pseudo-spectral algorithm in the periodic poloidal and axial coordinates. A leapfrog algorithm is used to advance wave-like terms; advective terms are treated with a simple predictor–corrector method. The semi-implicit term is introduced as a simple modification to the momentum equation. Dissipation is treated implicitly. The resulting algorithm is unconditionally stable with respect to normal modes. A general discussion of the semi-implicit method is given, and specific forms of the semi-implicit operator are compared in physically relevant test cases. Long-time simulations are presented.

1. INTRODUCTION

Nonlinear magnetohydrodynamic systems often evolve on time scales that are long compared to those associated with the fastest normal modes of the system. Examples are: the growth and saturation of resistive instabilities [1]; relaxation, sustainment, and flux generation in the reversed field pinch [2, 3]; low frequency current drive models for fusion plasmas [4]; the onset of the tokamak major disruption [5]; and, the response of the solar coronal magnetic field to slow photospheric motion [6]. These phenomena are dominated by low frequency, long wavelength motions that may have locally large spatial gradients. Their numerical

0021-9991/87 $3.00

simulation, generally required because of their nonlinear and multidimensional nature, is an especially difficult problem. Adequate spatial resolution requires that many mesh points (modes) be used. Stability restrictions placed on explicit temporal approximations then result in uneconomically small time-steps, while the fully implicit treatement of nonlinear terms either requires iteration (as in finite difference methods [7]), or results in unacceptably large matrices (as in spectral methods).

One approach to performing such computations is to employ analytical approximations, such as reduced equations [8] or incompressible models, that eliminate the fastest normal modes from the system. Reduced equations have been successfully applied to specific magnetoplasma configurations. However, codes based on specialized equations may be of limited applicability. Incompressible models remove the fast magnetosonic mode, but may also eliminate important features of the physical system [9]. Another approach is to apply implicit methods to only certain terms in the governing equations. For example, an implicit pressure advance may be used to eliminate the fast magnetosonic mode while retaining long wavelength compressibility [10]. The time step remains limited by the shear Alfvén wave, which still evolves rapidly compared to the phenomena of interest.

Recently, a new class of methods for solving the time-dependent MHD equations based on an algorithm developed for long-range weather simulation [11] has been introduced [12, 13]. These semi-implicit algorithms allow very large time-steps, yet avoid the complexity and large memory requirements associated with implicit methods. In the semi-implicit methods for MHD new terms are added to the time-discretized equations that do not affect the consistency of the solution, yet provide a simple and efficient means of enhancing stability. This technique was first applied to the MHD equations in order to eliminate the fast mode time-step constraint [12]. Subsequently, this procedure was extended to eliminate the shear Alfvén time-step constraint as well [13]. This method is unconditionally stable with respect to all Alfvén modes and consequently permits such large time-steps that accuracy becomes the most important considerations in the choice of step size. The semi-implicit method may be implemented using a variety of different time advance schemes and forms for the semi-implicit terms. The choice of the particular semi-implicit method, both in the order of accuracy and the form of the semi-implicit terms, can affect the size of the allowable time-step. The proper choices can lead to improved efficiency and accuracy for long-time scale three-dimensional nonlinear MHD computations.

This paper serves as an amplification and extension of our previous work [13]. Its purpose is fourfold: to present a particular three-dimensional semi-implicit algorithm that has proven useful in the simulation of the long-time scale MHD phenomena; to provide additional insight into the use and application of the semi-implicit method; to exhibit the accuracy of the semi-implicit method; and, to present several specific examples of nonlinear MHD simulations that demonstrate the power and utility of the semi-implicit algorithm. The paper is organized as follows: in Section 2 we present the physical model, and the spatial and temporal

approximations employed in the simulation; in Section 3 we present a brief general discussion of the semi-implicit method and display two particular forms of the semi-implicit operator that we have found useful; in Section 4 we display the accuracy of the method by presenting linear and nonlinear examples using different time-steps, and with different semi-implicit operators. We also present long-time scale three-dimensional simulations in several magnetoplasma configurations. Section 5 contains the discussion and conclusions.

2. Computational Model

In this section we present the specific mathematical model addressed in this paper, and the spatial and temporal approximations employed in its numerical solution.

2.1. *Mathematical Model*

We are concerned with the low-frequency, long-wavelength motion of an electrically conducting fluid in the presence of a strong magnetic field. When the magnetic energy density is large compared with the internal energy density, as is the case for many applications, these motions are governed primarily by the interaction between the total Lorentz force acting on the fluid and the induced magnetic field due to fluid motion. The evolution of such a system is described by the (force-free) MHD equations, which, in a convenient set of nondimensional variables, can be written as

$$\frac{\partial \mathbf{A}}{\partial t} = S\mathbf{V} \times \mathbf{B} - \eta \mathbf{J}, \tag{1a}$$

$$\rho \frac{\partial \mathbf{V}}{\partial t} = -S\rho \mathbf{V} \cdot \nabla \mathbf{V} + S\mathbf{J} \times \mathbf{B} + \nu \nabla^2 \mathbf{V}, \tag{1b}$$

where $\mathbf{B}$ is the magnetic field measured in units of a characteristic field strength B_0, $\mathbf{V}$ is the fluid velocity measured in units of the Alfvén velocity $v_A = B_0/\sqrt{4\pi\rho_0}$, η is the resistivity measured in units of a characteristic resistivity η_0, length is measured in units of a characteristic length a, time is measured in units of the resistive diffusion time $\tau_R = 4\pi a^2/c^2\eta_0$, $\mathbf{A}$ is the vector potential, $\mathbf{J}$ is the current density, ρ is the mass density measured in units of ρ_0, and we have chosen a gauge such that the gradient of the electrostatic potential vanishes. In these units the Lundquist number $S = v_A \tau_R / a$ is the ratio of the resistive and Alfvén time scales, and the nondimensional viscosity coefficient is $\nu = \nu_0 \tau_R / a^2$, where ν_0 is the characteristic viscosity; ν measures the ratio of the resistive diffusion time to the viscous diffusion time. Consistent with the force-free assumption, we have ignored the effects of perturbed fluid pressure, assume the mass density to be uniform in space and time, and take $\rho = 1$.

Equations (1) are fully compressible, and describe both shear and compressional

Alfvén waves, as well as resistive instabilities and resistive and viscous damping. Their nonlinear evolution is particularly appropriate to the description of force-free relaxation in the reversed-field pinch (RFP) [14], and to other phenomena whose origin is primarily electromagnetic. Because of the widely separated time scales supported by these equations when S is large, their solution presents an extremely difficult test of any numerical method.

The mathematical model described here supports a wide variety of solutions ranging from global kink and tearing modes to high frequency, short wavelength turbulence. We emphasize that our goal is to simulate the long time scale, nonlinear, three-dimensional evolution of long wavelength, low frequency motions for which geometric effects such as magnetic shear, field line curvature, and finite boundaries are important. We therefore employ temporal approximations in cylindrical geometry that permit time steps far in excess of those allowed by explicit methods. We make no attempt to simultaneously model turbulence, for which high resolution, short time-step explicit methods are appropriate [15].

2.2. *Spatial Approximation*

We choose cylindrical coordinates (r, θ, z), $0 \leqslant r \leqslant r_{\max}$, $0 \leqslant \theta \leqslant 2\pi$, $0 \leqslant z \leqslant L$, and define the scale length a such that $r_{\max} = 1$. We further assume that the solutions of (1) are periodic in z with $L = 2\pi R$, where R is the aspect ratio. Then introducing the discrete mesh $\theta_j = 2\pi(j-1)/M$, $j = 1, 2, \ldots, M$; $z_k = 2\pi(k-1)\,R/N$, $k = 1, 2, \ldots, N$; any quantity can be represented as a finite Fourier series

$$f(r, \theta_j, z_k) = \sum_{m=-M/2+1}^{M/2} \sum_{n=-N/2+1}^{N/2} f_{m,n}(r)\, e^{i(m\theta_j + nz_k/R)}, \tag{2}$$

where the complex finite Fourier coefficients $f_{m,n}$ are defined as

$$f_{m,n}(r) = \frac{1}{MN} \sum_{j=1}^{M} \sum_{k=1}^{N} f(r, \theta_j, z_k)\, e^{-i(m\theta_j + nz_k/R)}, \tag{3}$$

and the reality of $f(r, \theta, z)$ requires that $f_{-m,-n} = f^*_{m,n}$. The representation (2) is chosen because of the periodic boundary conditions in θ and z, and the rapid convergence properties for smooth solutions [16].

Introducing (2) into (1) yields

$$\frac{\partial \mathbf{A}_{m,n}}{\partial t} = S(\mathbf{V} \times \mathbf{B})_{m,n} - (\eta \nabla \times \nabla \times \mathbf{A})_{m,n}, \tag{4a}$$

$$\frac{\partial \mathbf{V}_{m,n}}{\partial t} = -S(\mathbf{V} \cdot \nabla \mathbf{V})_{m,n} + S(\mathbf{J} \times \mathbf{B})_{m,n} + \nu(\nabla^2 \mathbf{V})_{m,n}, \tag{4b}$$

where $\mathbf{A}_{m,n}$ and $\mathbf{V}_{m,n}$ are the Fourier coefficients of the vector potential and velocity, and the subscript $(\,)_{m,n}$ on a nonlinear term or operator represents the finite Fourier transform of that term.

Equations (4) are a set of MN nonlinear partial differential equations in the radial coordinate, r, and the time, t, that describe the evolution of the complex Fourier coefficients $\mathbf{A}_{m,n}$ and $\mathbf{V}_{m,n}$. They are the equations that we solve numerically. The nonlinear terms appearing on the right-hand side of (4) are evaluated using a fully dealiased pseudospectral algorithm in combination with the fast-Fourier-transform (FFT). This has been adequately described elsewhere [17]. It remains to describe the radial approximation of the operators appearing on the right-hand side of (4).

The operator $(\eta\mathbf{J})_{m,n} = (\eta\nabla\times\nabla\times\mathbf{A})_{m,n}$ appearing in (4a) couples Fourier modes if $\eta = \eta(r, \theta, z)$ and must be represented by a convolution sum, rendering an implicit treatment difficult. For this reason we limit the resistivity to have radial variation only. (This is not a fundamental limitation, as semi-implicit methods could be applied to this term [13].)

It proves convenient to introduce two staggered radial meshes [10, 18]. We define A_θ, A_z, B_r, $\mathbf{V}$, J_θ, J_z, and, using simple averaging, $(\mathbf{V}\times\mathbf{B})_\theta$, $(\mathbf{V}\times\mathbf{B})_z$, and $\mathbf{J}\times\mathbf{B}$ on the mesh $(r_i, i=1, I)$ such that $r_1 = -\Delta r/2$, $r_2 = \Delta r/2$, $(r_I + r_{I-1})/2 = 1$; and we define A_r, B_θ, B_z, J_r, and $(\mathbf{V}\times\mathbf{B})_r$ on the mesh $(r_{i+1/2}, i=1, I-1)$ such that $r_{i+1/2} = (r_i + r_{i+1})/2$ and $r_{I-1/2} = 1$. The magnetic field and current density are then defined in terms of finite curl operators on the two meshes

$$\begin{aligned}\mathbf{B} = \nabla_i\times\mathbf{A} = \hat{e}_r i\left[\frac{m}{r_i}A_{z_i} - kA_{\theta_i}\right] \\ - \hat{e}_\theta\left[\frac{1}{\Delta r_{i+1/2}}(A_{z_{i+1}} - A_{z_i}) - ikA_{r_{i+1/2}}\right] \\ + \hat{e}_z\left[\frac{r_{i+1}A_{\theta_{i+1}} - r_i A_{\theta i}}{r_{i+1/2}\Delta r_i} - \frac{im}{r_{i+1/2}}A_{r_{i+1/2}}\right],\end{aligned} \tag{5}$$

$$\begin{aligned}\mathbf{J} = \nabla_{i+1/2}\times\mathbf{B} = \hat{e}_r i\left[\frac{m}{r_{i+1/2}}B_{z_{i+1/2}} - kB_{\theta_{i+1/2}}\right] \\ - \hat{e}_\theta\left[\frac{1}{\Delta r_i}(B_{z_{i+1/2}} - B_{z_{i-1/2}}) - ikB_{r_i}\right] \\ + \hat{e}_z\left[\frac{r_{i+1/2}B_{\theta_{i+1/2}} - r_{i-1/2}B_{\theta_{i-1/2}}}{r_i\Delta r_i} - \frac{im}{r_i}B_{r_i}\right],\end{aligned} \tag{6}$$

where $k = n/R$, and the subscript $(\,)_{m,n}$ has been suppressed on all Fourier coefficients. These operators have the desirable property that their divergences vanish identically. Additionally, the double curl operator $\mathbf{J} = \nabla_{i+1/2}\times\nabla_i\times\mathbf{A}$ couples only nearest neighbor points on the appropriate radial meshes. The staggered mesh also allows boundary conditions to be introduced in a natural way, as described in Section 2.4.

2.3. *Temporal Approximation*

Since the linearized MHD equations exhibit wave-like solutions, it is natural to introduce leapfrog time discretization into Eq. (4), with **A** and **V** defined at staggered time intervals. This procedure is complicated by the fact that the term $\mathbf{V}\times\mathbf{B}$ on the right-hand side of (4a) contains variables defined at different time levels. This is not a problem when **V** is small, but as zero-order flows develop the algorithm becomes unstable. A similar problem arises in the treatment of the term $\mathbf{V}\cdot\nabla\mathbf{V}$ in Eq. (4b). We treat these terms separately with a simple predictor–corrector method. The resulting algorithm is

$$\frac{\mathbf{A}^* - \mathbf{A}^{n-1/2}}{\Delta t} = S(\mathbf{V}^n \times \mathbf{B}^{n-1/2}), \tag{7a}$$

$$\mathbf{B}^* = \nabla \times \mathbf{A}^*, \tag{7b}$$

$$\frac{\mathbf{A}^{n+1/2} - \mathbf{A}^{n-1/2}}{\Delta t} = S(\mathbf{V}^n \times \mathbf{B}^*) - \frac{\eta}{2}(\nabla \times \nabla \times \mathbf{A}^{n+1/2} + \mathbf{J}^{n-1/2}), \tag{7c}$$

$$\mathbf{B}^{n+1/2} = \nabla \times \mathbf{A}^{n+1/2}, \tag{7d}$$

$$\mathbf{J}^{n+1/2} = \nabla \times \mathbf{B}^{n+1/2}, \tag{7e}$$

$$\frac{\mathbf{V}^* - \mathbf{V}^n}{\Delta t} = -S\mathbf{V}^n \cdot \nabla \mathbf{V}^n, \tag{7f}$$

$$\frac{\mathbf{V}^{n+1} - \mathbf{V}^n}{\Delta t} = -S\mathbf{V}^* \cdot \nabla \mathbf{V}^* + S\mathbf{J}^{n+1/2} \times \mathbf{B}^{n+1/2} + \frac{1}{2}\nu(\nabla^2 \mathbf{V}^{n+1} + \nabla^2 \mathbf{V}^n), \tag{7g}$$

where we have again suppressed the subscripts $(\ )_{n,m}$, and have treated the dissipative terms implicitly to avoid severe time-step restrictions when η or ν are locally large. The quantities $\mathbf{A}^*$, $\mathbf{B}^*$, and $\mathbf{V}^*$ are provisional values introduced through the predictor steps (7a), (7b), and (7f). The algorithm defined above is second-order accurate in Δt for linearized normal modes (provided there is no equilibrium flow), but is formally first-order accurate. (A second-order predictor results in an unconditionally unstable algorithm.)

When (5) and (6) are introduced into (7c), the radial component of the vector potential at time level $n+1/2$ appears only algebrically, and can be eliminated from the system. Thus the induction equation reduces to two simultaneous equations for $A_\theta^{n+1/2}$ and $A_z^{n+1/2}$. Similarly, the vector Laplacian appearing in the equation of motion (7g) couples only the radial (r) and azimuthal (θ) components of $\mathbf{V}^{n+1}$. Thus only simple 2×2 block tridiagonal matrices need be inverted. The axial (z) component of **V** is advanced separately.

The algorithm (7) is linearly stable provided the conditions

$$|k_{\max} V_A \Delta t| < 2, \tag{8a}$$

$$|k_{\max} V \Delta t| < 1, \tag{8b}$$

are satisfied. Here k_{max} is the magnitude of the largest wave vector described by the simulation, V_A is the Alfvén velocity, V is the magnitude of the flow velocity, and Δt is the time step. Condition (8b) is required to stabilize the advective terms $\sim \mathbf{V} \cdot \nabla$, and is significant only when $V \sim V_A$. Condition (8a) arises from the wavelike normal modes of the system, and presents a severe restriction on the allowable time-step. The semi-implicit method eliminates this restriction, and allows the computation to proceed on the longer time scale defined by Eq. (8b). The introduction of the semi-implicit term into (7) will be discussed in Section 3.

2.4. *Boundary and Initial Conditions*

To effect a solution, Eqs. (4) must be supplemented by boundary and initial conditions. These are descibed below.

For our applications we have taken the initial conditions to be axisymmetric, one-dimensional solutions to the ideal MHD equilibrium equation $\mathbf{J} \times \mathbf{B} = 0$. Non-axisymmetric Fourier modes are introduced at small amplitude, either as random perturbations or through a data file. Unstable modes will then evolve allowing for the study of the long-time nonlinear behavior of the system.

At the origin $r = 0$, regularity requires that Fourier coefficients of a vector $\mathbf{U}$ corresponding to different values of the azimuthal mode number, m, be treated separately. In particular, at $r = 0$ we impose:

for $m = 0$,

$$\begin{aligned} &U_r, U_\theta \sim Cr, \\ &U_z \sim C_1 + C_2 r^2; \end{aligned} \tag{9a}$$

for $|m| = 1$,

$$\begin{aligned} &U_r, U_\theta \sim C_1 + C_2 r^2, \\ &U_z \sim Cr; \end{aligned} \tag{9b}$$

for $|m| > 1$,

$$\begin{aligned} &U_r, U_\theta \sim Cr^{m-1}, \\ &U_z \sim Cr^m. \end{aligned} \tag{9c}$$

In practice, these conditions are imposed only on the θ and z components; the radial components is then given as $U_r = iU_\theta$. This assures that the Cartesian components of $\mathbf{U}$ are unique at $r = 0$.

At the outer boundary we specify the $m = 0$, $n = 0$ components of the tangential electric field $\mathbf{E}_0(t) = E_{\theta_0}(t)\,\hat{e}_\theta + E_{z_0}(t)\,\hat{e}_z$. Then at the outer boundary the θ and z components of the vector potential satisfy the evolutionary equations

$$\hat{e}_r \times \frac{\partial \mathbf{A}_{m,n}}{\partial t} = -\hat{e}_r \times \mathbf{E}_0 \delta_{m,n}, \tag{10}$$

which, through the radial component of (5), assures that the outer boundary remains a flux surface. Because of the construction of the radial mesh, as described in Section 2.2, the radial component of **A** is self-consistently determined at the outer boundary without the need for a boundary condition.

In the absence of viscosity, the radial component of the velocity at the outer boundary is given by

$$V_r = \frac{(\mathbf{E} - \eta \mathbf{J}) \times \mathbf{B}}{SB^2}, \tag{11}$$

as long as V_r is negative (as is the case for most fusion applications); with viscosity, Eq. (11) can always be applied. Equation (11) is consistent with the Poynting flux arising from an applied electric field, and with Ohm's law provided $\mathbf{E} - \eta \mathbf{J}$ is orthogonal to **B**. In the presence of viscosity, the tangential components of **V** may be specified arbitrarily and are assumed to vanish.

3. The Semi-implicit Algorithm

As discussed in Section 2.3, the algorithm defined by Eq. (7) is restricted to small time-steps determined by Eq. (8a). Efforts to remove this restriction by a fully implicit treatment of the nonlinear wave-like terms $(\mathbf{V} \times \mathbf{B})_{m,n}$ and $(\mathbf{J} \times \mathbf{B})_{m,n}$ result in a coupling of all Fourier coefficients and requires the inversion of intractably large matrices. In the semi-implicit method we modify the original momentum Eq. (1b) by the addition of a linear term with a coefficient proportional to the time step. We thus replace (1b) with

$$\frac{\partial \mathbf{V}}{\partial t} = \mathbf{F} + \alpha \Delta t \mathbf{G} \cdot \frac{\partial \mathbf{V}}{\partial t}, \tag{12}$$

where **F** represents the right-hand side of (1b), α is a numerical constant, and **G** is the linear semi-implicit operator whose form is (at this point) arbitrary. The corresponding modification to the algorithm (7) is to replace (7g) with

$$\frac{\mathbf{V}^{n+1} - \mathbf{V}^n}{\Delta t} = \mathbf{F} + \alpha \mathbf{G} \cdot (\mathbf{V}^{n+1} - \mathbf{V}^n), \tag{13}$$

where **F** represents the right-hand side of (7g). Solution of Eq. (13) requires the inversion of the *linear* operator $\mathbf{I} - \alpha \mathbf{G} \Delta t$, where **I** is the identity operator. Furthermore, since **G** is linear, the Fourier coefficients remain decoupled. As shown in Ref. [13], suitable choices of α and **G** may remove the severe time-step restriction imposed by Eq. (8a).

In this section we discuss the properties of the modified system described by (1a) and (12) (including errors introduced by the semi-implicit term), demonstrate

heuristically the stabilizing properties of the method, and explicitly display two possible forms of the operator **G** suitable for the MHD equations. At this point, however, we note two properties of the method: (1) the original system is recovered in the limit $\Delta t \to 0$; and, (2) the physical system is unaffected in the limit $\partial \mathbf{V}/\partial t \to 0$. Thus, steady-state solutions obtained with the semi-implicit method are solutions of the original equations.

3.1. *General Considerations: Accuracy*

For the purposes of our heuristic analysis, we consider the simple linear system

$$\frac{\partial u}{\partial t} = \mathbf{B}v, \tag{14a}$$

$$\frac{\partial v}{\partial t} = \mathbf{A}u, \tag{14b}$$

where **A** and **B** are linear operators independent of time, and u and v are vectors. Equations (14a), (14b) can be combined to yield a wave equation for v,

$$\frac{\partial^2 v}{\partial t^2} = \mathbf{L}v, \tag{15}$$

where $\mathbf{L} = \mathbf{AB}$. An identical equation holds for u if **A** and **B** commute. Equations (14a), (14b) are analogous to (1a), (1b), and Eq. (15) is analogous to the linearized MHD wave equation

$$\frac{\partial^2 \mathbf{V}}{\partial t^2} = \nabla \times \nabla \times (\mathbf{V} \times \mathbf{B}_0) \times \mathbf{B}_0. \tag{16}$$

For simplicity, we assume that **L** has a complete set of orthonormal eigenvectors $\{\xi_k\}$, with corresponding eigenvalues $\{-\omega_k^2\}$. Then expanding v in the eigenvectors of **L**, we find that the normal modes of (15) evolve according to

$$\frac{d^2 a_k}{dt^2} = -\omega_k^2 a_k, \tag{17}$$

where the a_k are the coefficients in the normal mode expansion of v.

Now consider the modified system

$$\frac{\partial u}{\partial t} = \mathbf{B}v, \tag{18a}$$

$$\frac{\partial v}{\partial t} = \mathbf{A}u + \alpha \Delta t \mathbf{G} \frac{\partial v}{\partial t}, \tag{18b}$$

where **G** is an operator with complete, orthonormal eigenvectors $\{\zeta_k\}$ and eigenvalues $\{-\sigma_k^2\}$. Equations (18) correspond to Eqs. (1a) and (12) of the previous sections. Combining (18a), (18b) we find, analogous to (15),

$$(1-\alpha\Delta t\mathbf{G})\frac{\partial^2 v}{\partial t^2}=\mathbf{L}v, \tag{19}$$

which is the wave equation for the modified system.

We now inquire to what extent the solutions of (19) correspond to those of the original Eq. (15). To this end we expand v in the eigenvectors ξ_k of **L** (again with expansion coefficients a_k), determine the effect of **G** operating these eigenvectors by expanding them in the eigenvectors ζ_k of **G**, and take the inner product of the resulting equation with ξ_m. The equations for the original normal modes can then be written as

$$\ddot{a}_m=-\frac{\omega_m^2}{1+\alpha\Delta t\sum_l \sigma_l^2|b_{ml}|^2}a_m$$

$$-\frac{\alpha\Delta t}{1+\alpha\Delta t\sum_l \sigma_l^2|b_{ml}|^2}\sum_{k\neq m}\ddot{a}_k\sum_l \sigma_l^2 b_{kl}b_{ml}^*, \qquad m=0,\,1,\ldots, \tag{20}$$

where $b_{km}=(\zeta_m,\,\xi_k)$ is the inner product of the mth eigenvector of **G** with the kth eigenvector of **L**, and ( )* denotes the complex conjugate. Thus the evolution of the a_k in the modified system differs from their evolution in the original system, as described by Eq. (17).

When $\Delta t\to 0$, (20) reduces to (17). For finite Δt there are two sources of error. First, the equations for the a_k are coupled, so that they do not evolve independently. It is thus desirable to choose **G** such that its eigenvectors are almost parallel to those of **L**; then $b_{km}=C_k\delta_{km}+\varepsilon_{km}$ with $C_k\sim 1$, $\varepsilon_{km}\ll 1$. The choice $\mathbf{G}=\mathbf{L}$ is obvious, but, as pointed out in Ref. [13], this can defeat the purpose of the method, since it requires inversion of the same operator as in a fully implicit method. A more relevant case is one in which Δt is large and we wish to describe only a subset of the normal modes accurately, say, for $0\leqslant m\leqslant K$. It is then desirable to choose **G** such that its eigenvectors correspond closely to those of **L** for only this subset, and may be arbitrarily oriented for m outside this range. Then, the eigenvectors of **G** within the subset will also be orthogonal to those of **L** outside the subset, so that the normal mode Eqs. (20) decouple for $0\leqslant m\leqslant K$. The remaining modes cannot affect the modes of interest.

The second source of error arises from the term $1+\alpha\Delta t\sum_l \sigma_l^2|b_{ml}|^2$ appearing in (20). Thus, aside from questions of numerical stability, we must choose Δt small enough that $|\alpha\sigma_m^2\Delta t|\ll 1$ for modes of interest. This conclusion is independent of the correspondence of σ_m^2 to ω_m^2; however, the problem is amplified if $\sigma_m^2\gg\omega_m^2$. We expect that the closer **G** approximates **L** for modes of interest, the closer will be the correspondence between σ_m^2 and ω_m^2. We will return to this point when we discuss specific examples in Section 4.

We thus arrive at the almost self-evident conclusion that **G** should closely approximate **L** for the modes of interest if they are to be accurately represented for large Δt. This is particularly important and difficult for MHD where the operator **L** is anisotropic; **G** should mimic these anisotropies as closely as possible.

3.2. *General Considerations: Stability*

For simplicity of analysis, we consider the case where ξ_k is simultaneously an eigenvector of **A** and **B** with eigenvalue $i\omega_k$. Then assuming that **G** closely approximates **L**, as discussed in Section 3.1, and applying the leapfrog algorithm to (18a), (18b), we have

$$\left.\begin{aligned} \frac{c_k^{n+1/2} - c_k^{n-1/2}}{\Delta t} &= i\omega_k a_k^n \\ (1+\alpha\sigma_k^2\Delta t)\frac{a_k^{n+1} - a_k^n}{\Delta t} &= i\omega_k c_k^{n+1/2} \end{aligned}\right\} \quad k=0,\,1,\,2,\ldots,\,N, \tag{21}$$

where the $c_k = (\xi_k, u)$ are the expansion coefficients for u, and the a_k are, as before, the expansion coefficients for v. These are the analogues of equations (7a)–(7f) and (13). A straightforward stability analysis shows that (21) is unconditionally stable provided the condition

$$\alpha\sigma_k^2\Delta t \geqslant \frac{\omega_k^2\Delta t^2}{4} - 1 \tag{22}$$

holds for all k in the calculation. This serves to determine the coefficient α. When $\omega_k^2\Delta t^2 < 4$, (21) is explicitly stable and α is set to zero.

If we further assume that **L** possesses a maximum eigenvalue $\omega_{\max}^2$, and that $\sigma_k^2 \sim \omega_k^2$, then the accuracy condition $\alpha\sigma_k^2\Delta t \ll 1$ for modes of interest, discussed in Section 3.1, reduces to $|\omega_k\Delta t| \leqslant 2$, i.e., the time step should be chosen such that the modes of interest are explicitly stable. Since these modes are presumably low frequency, a considerable advantage is still gained over purely explicit methods, as will be demonstrated in Section 4. The maximum time-step is thus dictated by accuracy, rather than stability, considerations.

We note that, in the wave equation for normal modes, i.e.,

$$(1+\alpha\sigma_k^2\Delta t)\frac{\partial^2 a_k}{\partial t^2} = -\omega_k^2 a_k, \tag{23}$$

the role of the semi-implicit term is to effectively increase the inertia of the system as a function of k. This is heuristically the means by which stability is achieved. (This is especially clear for the special case $\sigma_k^2 = k^2$.) Thus low-k modes are relatively unaffected, while the frequencies of high-k modes are modified such as to render them stable. This k-dependent inertia is achieved through the spatial depen-

dence of the operator **G**, and not by enhancing the overall mass of the system, as in previous methods [19].

We close this section by noting that the semi-implicit algorithm, as given by Eq. (21), introduces no damping. Since the dispersion relation for the high-k modes may be considerably modified, it may be advantageous to introduce some additional diffusion, e.g., through the viscous term in Eq. (1b).

3.3. *Semi-implicit Terms for MHD*

In Ref. [13] a semi-implicit term was given for the MHD equations. That term was obtained from the linearized MHD operator

$$\mathbf{LV} = \nabla \times \nabla \times (\mathbf{V} \times \mathbf{B}_0) \times \mathbf{B}_0 \tag{24}$$

by replacing $\mathbf{B}_0$ with a constant vector $\mathbf{C}_0$, and then retaining only terms proportional to C_α^2, where $\alpha = r, \theta, z$. However, this form couples all components of the velocity. In the present case we further ignore any coupling between V_z and (V_r, V_θ). This allows us to retain 2×2 block tridiagonal structure of the algorithm. The exact form of the operator is detailed in the Appendix. We find that, in analogy with (22), and with results obtained in Ref. [13], stability results provided

$$C_\alpha^2 k_{\max}^2 \Delta t^2 \geqslant \frac{S^2 B_\alpha^2 k_{\max}^2 \Delta t^2}{4} - 1 \tag{25}$$

is simultaneously satisfied for $\alpha = r, \theta, z$.

The form of the semi-implicit term based on (24), and displayed in the Appendix, contains much of the anisotropic character of the original MHD equations. The essence of stability is provided by the elliptic part of that operator. We are thus led to try a second, extremely simple form for the operator, i.e.,

$$\mathbf{GV} = \nabla^2 \mathbf{V}. \tag{26}$$

The algorithm based on Eq. (26) is very easy to implement. Explicit codes already containing implicit viscosity can be modified to be semi-implicit with a minimum of programming effort; the viscosity is merely explicitly subtracted at the old time level. The algorithm is stable provided

$$\nu k_{\max}^2 \Delta t > \frac{S^2 B^2 k_{\max}^2 \Delta t^2}{4} - 1, \tag{27}$$

where ν is the "viscosity" coefficient, and B is the magnitude of the magnetic field. (The resulting algorithm is no longer dissipative.) However, the anisotropy inherent in the original MHD operator is not included, and will affect accuracy. [Note that

In the following section we give specific comparison between results obtained with the anisotropic term based on (24), and with the isotropic term (26), for relevant MHD problems.

4. EXAMPLES

In this section we present several examples of computations performed with the semi-implicit MHD algorithm described in the previous sections. The purpose of these examples is to demonstrate the accuracy and power of the method, and to provide a comparison between different forms of the semi-implicit operator. Detailed physics studies will be presented in future publications.

4.1. *Torsional Alfvén Waves*

As mentioned previously, the MHD equations support a wide variety of linearly stable normal modes. A particularly simple test case is that of torsional (shear) Alfvén waves in a uniform axial magnetic field (with $B_{z_{0,0}} = 1$). These modes are characterized by poloidal mode number $m = 0$ and arbitrary axial mode number n. They propagate parallel to the zero-order field, with each field line oscillating independently (i.e., independent of radius) at frequency $\omega_n = n/R$, where R is the aspect ratio. The anisotropic nature of these modes provide a simple yet demanding test of the form of the semi-implicit operator.

The initial conditions for this case are

$$\mathbf{B}_{0,0} = B_{z_{0,0}} \hat{e}_z, \tag{28a}$$

$$V_{\theta_{0,1}} = V_{\theta_{0,-1}} = \varepsilon r(1-r), \tag{28b}$$

$$B_{\theta_{0,1}} = B_{\theta_{0,-1}} = 0, \tag{28c}$$

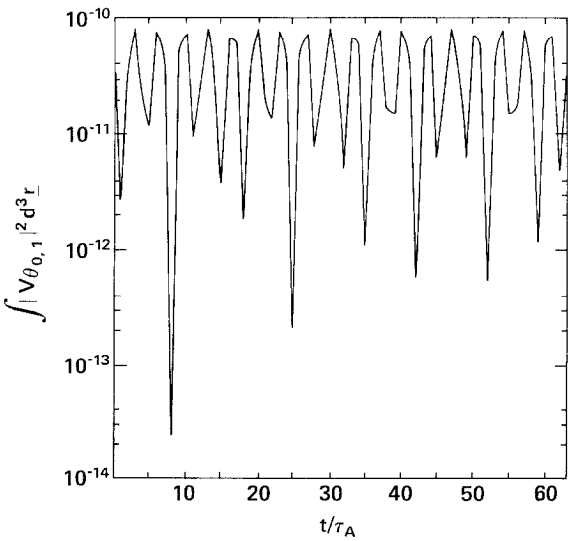

FIG. 1. Poloidal kinetic energy versus time for the $m = 0$, $n = 1$ standing Alfvén wave using the anisotropic semi-implicit operator. The time step is $\Delta t = \tau_A$, and the resulting period is $T = 6.81\ \tau_A$. (The analytic value is $T = 2\pi\tau_A$.)

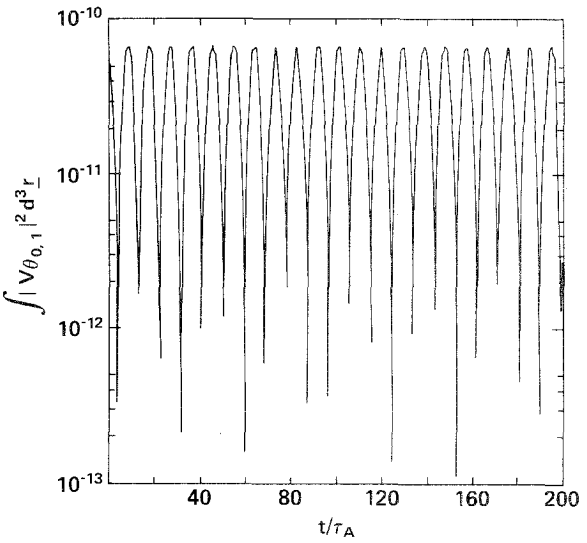

FIG. 2. The same case as shown in Fig. 1, except using the isotropic semi-implicit operator. With $\Delta t = \tau_A$, the period is $T = 19.05\,\tau_A$.

where $\varepsilon \ll 1$; we have perturbed both the $(m = 0, n = 1)$ and $(m = 0, n = -1)$ modes to obtain a standing wave solution, and have chosen $n = 1$ to obtain the primary (longest wavelength) mode. With aspect ratio $R = 1$, this mode should oscillate at frequency $\omega_1 = 1$ (i.e., have period $T_1 = 2\pi$ Alfvén times). We use a mesh of 65 radial points and 16 axial points, and advance the equations forward in time using the algorithm (7a)–(7f) and (13).

The results of this are shown in Figs. 1–3. In Fig. 1 we plot the kinetic energy versus time (measured in units of Alfvén times) for the case $\Delta t = 1$ (corresponding to one radial Alfvén transit time), using the anisotropic semi-implicit operator based on Eq. (24). The period of oscillations is $6.81\tau_A$, very close to the analytic value, even though the time step is over 30 times larger than would be allowed by an explicit algorithm. In Fig. 2 we show the results for the same parameters, but using the isotropic semi-implicit operator, Eq. (26). We find that the period is $19.05\tau_A$, too large by a factor of about 3. When the time step is reduced to $\Delta t = 0.1$, the $T = 6.41$ is obtained, as shown in Fig. 3. (This time step is still over 3 times larger than the explicit limit.) We again note that the semi-implicit method introduces no damping.

The error introduced by the isotropic operator (26) can be understood qualitatively by determining the numerical dispersion. From (21) we find that the dispersion relation for the algorithm can be written as

$$\tan^2 \frac{\omega \Delta t}{2} = \frac{\beta_k^2}{4 - \beta_k^2}, \tag{29}$$

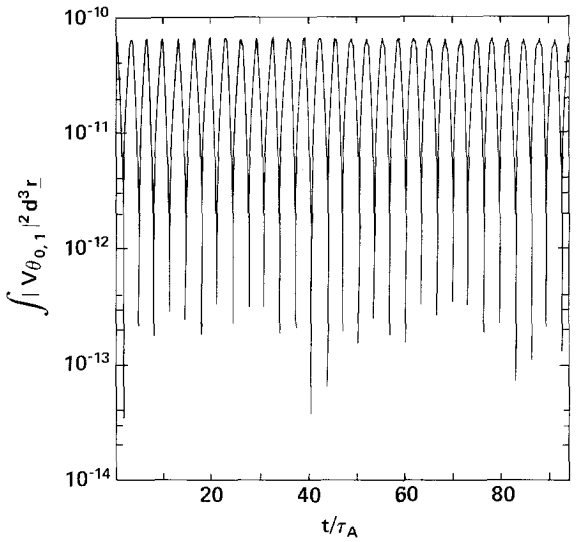

FIG. 3. The same case as Fig. 2, except with $\Delta t = 0.1\ \tau_A$. Now the period is $T = 6.41\ \tau_A$.

where ω is the frequency determined by the algorithm, and

$$\beta_k^2 = \frac{\omega_k^2 \Delta t^2}{1 + \alpha \sigma_k^2 \Delta t}. \tag{30}$$

In this expression, ω_k is the analytic frequency. From (22), stability requires $\beta_{k_{\max}}^2 \leqslant 4$. For simplicity we choose $\beta_{k_{\max}}^2 = 4$, and assume that $\sigma_{\max} \approx \omega_{\max}$. Then when $\omega_{\max} \Delta t \gg 1$, Eq. (29) can be rewritten as

$$\tan^2 \frac{\omega \Delta t}{2} = \frac{(\omega_k \Delta t/2)^2}{1 + (\sigma_k^2 - \omega_k^2)(\Delta t/2)^2}. \tag{31}$$

When $\sigma_k = \omega_k$, Eq. (31) is identical with that obtained with a second order accurate implicit method. This is the case for the anisotropic operator (24), since it only feels disturbances parallel to the magnetic field. However, the isotropic operator (26) also measures the radial variation of the mode, which physically plays no role in determining the frequency. In this case $\sigma_k^2 > \omega_k^2$ and a reduction in the computed frequency results.

4.2. *Growth and Saturation of Resistive Instabilities*

Resistive instabilities present a difficult computational problem due to their slow growth and radial structure, and have been a prime candidate for long time-step algorithms [7, 10, 20] and reduced models [5, 8]. Here we apply the semi-implicit method to the linear growth and nonlinear saturation of these modes.

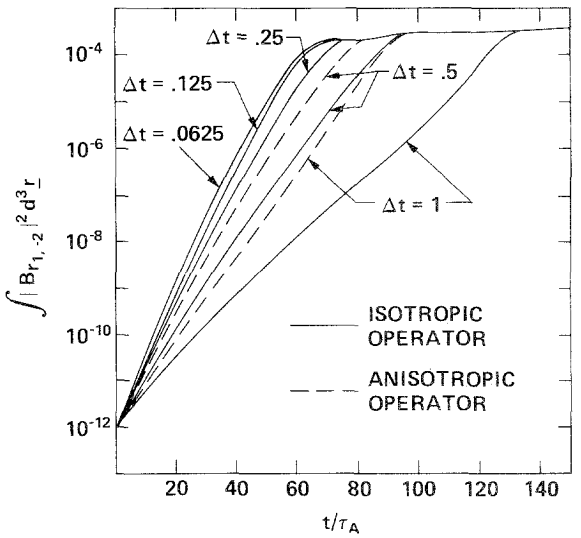

FIG. 4. Radial magnetic energy versus time for the unstable $m=1$, $n=-2$ tearing mode for various time-steps using both the isotropic (solid lines) and anisotropic (dashed lines) forms of the semi-implicit operator.

We pose an initial value problem where the initial equilibrium magnetic fields are given by the safety factor profile

$$q(r) \equiv \frac{rB_{z_{0,0}}}{RB_{\theta_{0,0}}} = 0.4(1 - 1.8748r^2 + 0.83232r^4), \tag{32}$$

and are characteristic of the magnetic fields in the Reversed-Field Pinch (RFP). For the cases presented here, we choose $R=1$, and take the Lundquist number $S=10^3$. The profile (32) has been studied previously [9], and is known to be unstable to a nonresonant $m=1$, $n=-2$ mode, which we perturb with a linear eigenfunction of amplitude $(B_{r_{1,-2}})_{\max}/(B_{z_{0,0}})_{\max}=10^{-5}$. The nonlinear MHD equations are then advanced in time on a $65\times 8\times 16$ mesh for various time steps, using both isotropic and anisotropic semi-implicit operators, to determine the accuracy of the method.

The results of this study are shown in Fig. 4, where we plot the energy in the radial magnetic field of the unstable $(1,-2)$ mode as a function of time. The simulations are performed for 150 Alfvén times (0.15 resistive diffusion times at $S=10^3$). Results obtained with the isotropic operator are shown as solid curves, those obtained with the anisotropic operator as dashed curves. For both operators, unstable modes were found to grow linearly and then saturate. It is apparent that, in terms of linear growth rate, the anisotropic operator can tolerate about twice the time step as the isotropic operator, for the same accuracy. Both methods seem to require $\Delta t \leqslant 0.5$ for reasonable agreement with known results. This corresponds to

$\gamma \Delta t \lesssim 0.05$, and is consistent with the requirements placed on fully implicit solutions of the linearized equations [21].

We note that, while differences are observed in the linear phase, the nonlinear saturated state obtained in these runs appears to be independent of size of the time step, or of the form of the semi-implicit operator. This may be because in this state $\partial/\partial t \to 0$, so that the remarks of Section 3 become relevant.

Each of the runs presented in Fig. 2 required less than 10 minutes of CPU time on a CRAY-I computer.

4.3. *Long Time-Scale Simulations*

In the previous section we presented examples of the computation of the linear growth and nonlinear saturation of a single unstable mode. In many cases of interest, several unstable modes evolving simultaneously can affect the overall saturation. Perhaps more importantly, their nonlinear interaction for times well beyond that required for saturation may reveal new physical phenomena. Such computations have provided the motivation for the development of the semi-implicit method. In this section we give examples of the simulation of such an effect that demonstrates the full power of the method. These calculations are performed with both the anisotropic and isotropic semi-implicit operators to compare and constrast their effect on the nonlinear physics.

We consider the equilibrium profile given by Eq. (32), which we perturb with both the $(m=1, n=-1)$ and $(m=1, n=-2)$ modes. We sustain the current by applying an average axial electric field at the wall that is constant in time. The poloidal average electric field at the wall is set to zero so as to conserve toroidal flux. The resistivity is constant in space and time, with Lundquist number $S=10^3$. With unit aspect ratio, the spatial mesh is 65 radial, 8 poloidal, and 16 axial points. This case has been the subject of a previous study [9], where its nonlinear evolution was computed for up to 200 Alfvén times (0.2 resistive diffusion times) with several nonlinear 3-D MHD codes. There it was found that the nonlinear growth and saturation of the unstable nonresonant $(1, -2)$ mode led to the generation and sustainment of an average reversed axial field (B_z) at the wall, as is observed in reversed-field pinch (RFP) experiments. These simulations indicated the attainment of a steady field-reversed state dominated by an $m=1$, $n=-2$ helical perturbation that was maintained against resistive diffusion by finite flow.

Using the semi-implicit method we have computed the nonlinear evolution of this case for times in excess of one resistive diffusion time (>1000 Alfvén times). In Fig. 5 we plot the energy in various modes as a function of time (measured in resistive times) for a simulation using the *anisotropic* form of the semi-implicit operator. The initially unstable nonresonant $(m=1, n=-2)$ mode grows and saturates in about 0.02 resistive times, producing a helical state in agreement with previous results. However, this state is in turn unstable to the resonant $(1, -3)$ mode, which saturates in about 0.1 resistive times at an amplitude approximately equal to that of the $(1, -2)$. The $(1, -2)$ and $(1, -3)$ then proceed to periodically exchange energy for ~ 0.4 resistive times, resulting in a time-dependent, field-rever-

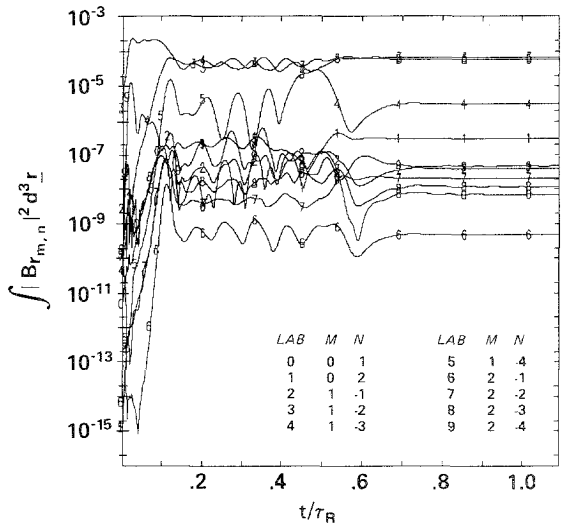

FIG. 5. Radial magnetic energy in various Fourier modes as a function of time (measured in resistive diffusion times) for a long-time RFP simulation with $S = 10^3$ using the anisotropic semi-implicit operator.

sed state. At $t \approx 0.5\tau_R$ a further nonlinear transition occurs, with the $(1, -3)$ and $(1, -4)$ modes interchanging roles. For $t \gtrsim 0.7\tau_R$ a fully three-dimensional resistive steady state results.

The nonlinear periodic energy exchange between the $(1, -2)$ and $(1, -3)$ modes occurring for $0.15\tau_R \lesssim t \lesssim 0.5\tau_R$ can be understood by considering $q(0)$, the value of the safety factor at $r = 0$. In Fig. 6 this quantity is plotted as a function of time.

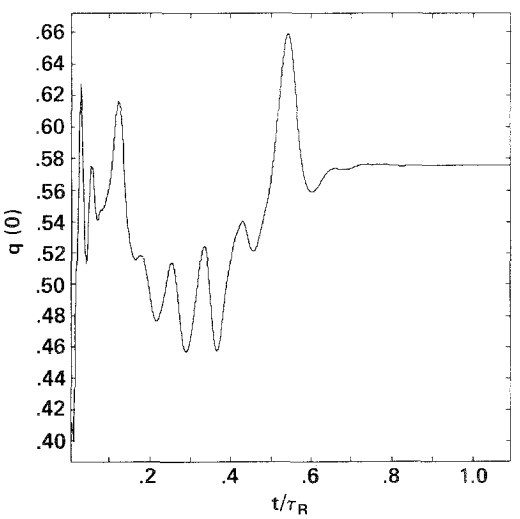

FIG. 6. Safety factor at $r = 0$ versus time for the case shown in Fig. 5.

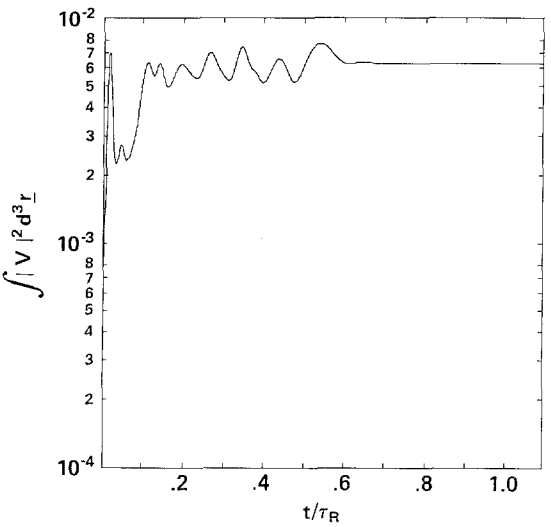

FIG. 7. Total kinetic energy versus time for the case shown in Fig. 5.

Initially, $q(0) < 0.5$, so that the unstable $(1, -2)$ mode is resonant from above. As is well known [2], the growth of such a mode raises $q(0)$ ("second reconnection"), increasing the shear, and stabilizing the mode. This behavior is seen at early times ($t < 0.1\tau_R$) in Fig. 6. However, this profile modification is sufficient to destabilize the resonant $(1, -3)$ mode, whose evolution is such as to lower $q(0)$, i.e., to remove the unstable resonance ("first reconnection") [2]. This is seen in Fig. 6 for $0.1\tau_R \lesssim t \lesssim 0.2\tau_R$. The achievement of $q(0) < 0.5$ again destabilizes the $(1, -2)$, causing $q(0)$

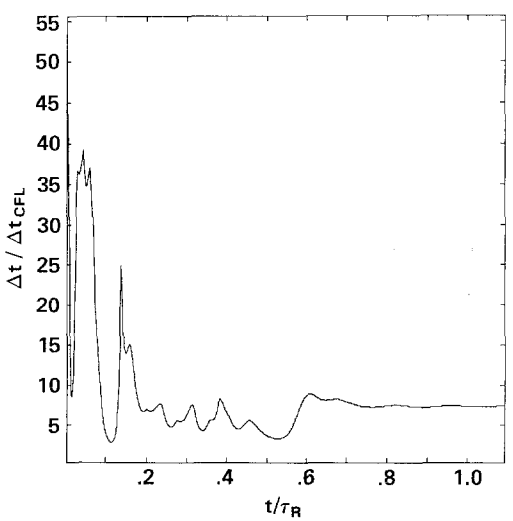

FIG. 8. $\Delta t/\Delta t_{CFL}$, the ratio of the actual time-step to that determined by the CFL stability limit, versus time for the case shown in Fig. 5.

to increase, which in turn destabilizes the $(1, -3)$, causing $q(0)$ to decrease. This periodic oscillation about $q(0) = 0.5$ is apparent in Fig. 6 for $0.2\tau_R \lesssim t \lesssim 0.5\tau_R$. Finally, at $t \approx 0.5\tau_R$ the interchange of the $(1, -3)$ and $(1, -4)$ causes $q(0)$ to increase abruptly, followed by the attainment of a resistive steady state. This second nonlinear transition is as yet not fully understood.

In Fig. 7 we plot the total fluid kinetic energy as a function of time for this case. Good agreement with previous results for $t \lesssim 0.2\tau_R$ (the extent of the previous calculations) is seen by comparison with Fig. (6b) of Ref. [9].

In Fig. 8 we plot $\Delta t/\Delta t_{CFL}$, the ratio of the actual time-step to the time-step that would be required by a fully explicit calculation. The actual time-step is adjusted throughout the run to assure that Eq. (8b), the advective Courant limit, is satisfied. Initially we have taken $\Delta t = 0.5\tau_A$. The time step then decreases as zero-order flows develop from both the nonlinear instabilities and the radial Poynting flux, Eq. (11). A close correspondence is seen between the "peaks" of Fig. 7 and the "valleys" of Fig. 8. During the initial nonlinear state $\Delta t \approx 5\Delta t_{CFL}$ is attained; in the long-time nonlinear phase, $\Delta t \approx 7\Delta t_{CFL}$.

In Fig. 9 we plot the modal energy versus time for the same case, except here we have employed the *isotropic* semi-implicit operator $\nabla^2 \partial \mathbf{V}/\partial t$. Note that this calculation has been run for 1.3 resistive diffusion times. Again we see the initial generation of a $(1, -2)$ helical state, the destabilization of the $(1, -3)$ mode, the periodic energy exchange between the $(1, -2)$ and $(1, -3)$ modes, the interchange of the roles of the $(1, -3)$ and $(1, -4)$, and the eventual approach to a three-dimensional resistive steady state. The final distribution of modal energy is the same

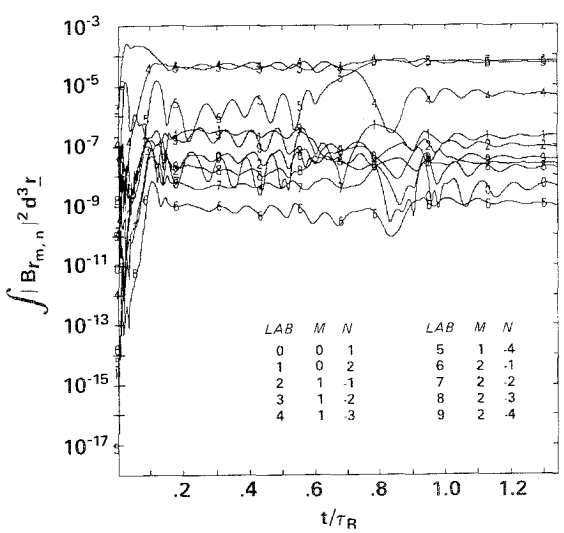

FIG. 9. Radial magnetic energy in various Fourier modes as a function of time for the same nonlinear case, except using the isotropic semi-implicit operator. Note that the same nonlinear phenomena occur as in Fig. 5; the time scales here are lengthened by ~30%.

for both anisotropic and isotropic semi-implicit operators. The primary difference between the cases is that all time scales, including the time to achieve steady state, seem to be lengthened by approximately 30% when the isotropic operator is used. This results from the difference in eigenvalues between the isotropic semi-implicit operator and the anisotropic MHD operator, as discussed in Sections 4.1 and 4.2, and not from inaccuracies in the high k dynamics.

The calculations presented here required approximately 2 h of time on a CRAY-I computer, and spanned slightly more than one resistive diffusion time. For the same spatial resolution, one of the explicit calculations [16] reported in Ref. [9] required approximately 20 h of CRAY-I time to compute for 0.2 resistive diffusion times. We estimate that each of the calculations presented in this section would require more than 100 hours of CRAY-I CPU time if performed with previous explicit methods [16]. The power of the semi-implicit method is self-evident.

4.4. *The Effect of Nonlinear Advection*

Many of the well-known difficulties occurring in computational hydrodynamics and MHD arise from the presence of the advective term $\mathbf{V}\cdot\nabla\mathbf{V}$ in the momentum equation. Among these difficulties are the generation of shock waves and the onset

boundary conditions, it is often convenient to remove this term from the model [18]. This is generally justified on the grounds that the velocity, which is viewed as a means by which the system moves from one equilibrium state to another, remains small throughout the evolution of the system. Since the inclusion of this term in the

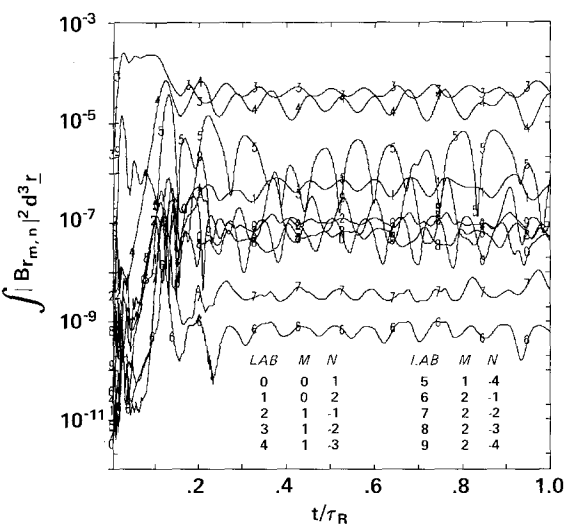

FIG. 10. The same as Fig. 5 (anisotropic semi-implicit operator) except that the term $\mathbf{V}\cdot\nabla\mathbf{V}$ has been set to zero throughout the simulation.

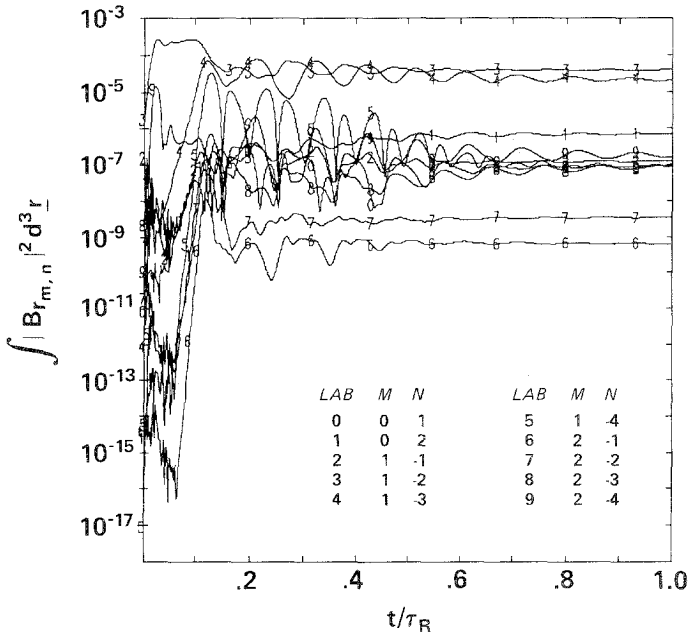

FIG. 11. The same as Fig. 9 (isotropic semi-implicit operator) except that the term $\mathbf{V}\cdot\nabla\mathbf{V}$ has been set to zero throughout the simulation.

present algorithm requires an additional 18 three-dimensional FFTs to be performed, its neglect would result in a more efficient computation. We thus enquire to what extent the neglect of this term affects the long-time scale nonlinear physics that we are attempting to model.

The results of these computations are shown in Figs. 10 and 11, where we plot the modal energy as a function of time for both the anisotropic (Fig. 10) and the isotropic (Fig. 11) semi-implicit operators *excluding* the term $\mathbf{V}\cdot\nabla\mathbf{V}$ from the equation of motion. Note that, for both cases, the final nonlinear interchange between the $(1, -3)$ and $(1, -4)$ modes does not occur; rather the periodic energy exchange between the $(1, -2)$ and $(1, -3)$ continues throughout the calculations. The final distribution of energy among the modes differs significantly according to the inclusion of $\mathbf{V}\cdot\nabla\mathbf{V}$. In the case of the anisotropic operator, Figs. 5 and 10, a resistive steady-state is not attained unless $\mathbf{V}\cdot\nabla\mathbf{V}$ is included. Thus the details of the nonlinear evolution differ significantly between the models.

On the other hand, the time evolution of global quantities such as the field reversal parameter $F = B_z(a)/B_{z_{ave}}$ are qualitatively unaffected by the absence of $\mathbf{V}\cdot\nabla\mathbf{V}$. This is illustrated in Fig. 12a–d, where we plot F as a function of time for the four cases presented in this and the previous section. In all cases, a time average reversed state with $F \cong -0.075$ is reached and maintained indefinitely. Thus, while the basic RFP dynamo mechanism is unaffected, the details of the relaxation process are altered by the removal of $\mathbf{V}\cdot\nabla\mathbf{V}$ from the model.

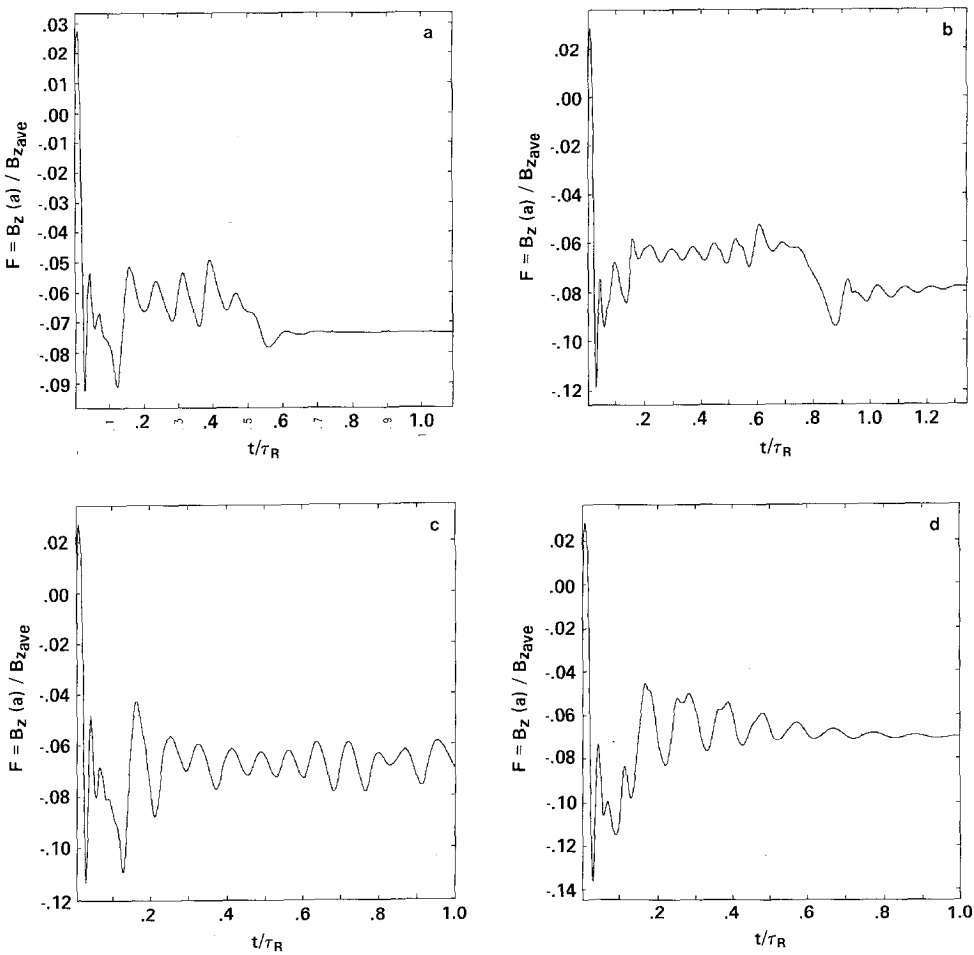

FIG. 12. Field reversal parameter $F = B_z(a)/B_{z_{ave}}$ versus time for the four cases presented in Sections 4.3 and 4.4: (a) anisotropic *with* $\mathbf{V}\cdot\nabla\mathbf{V}$; (b) isotropic *with* $\mathbf{V}\cdot\nabla\mathbf{V}$; (c) anisotropic *without* $\mathbf{V}\cdot\nabla\mathbf{V}$; (d) isotropic *without* $\mathbf{V}\cdot\nabla\mathbf{V}$.

5. SUMMARY AND CONCLUSIONS

We have presented a simple, accurate, and efficient algorithm for the long-time-scale numerical simulation of long wavelength, low frequency, MHD motions for which geometric effects are important. The algorithm incorporates nonideal, time-dependent boundary conditions in a natural way, and is thus appropriate for the dynamical simulation of systems driven by low frequency external agencies. Resistivity and viscosity are included in the model.

We have presented a general discussion of the semi-implicit algorithm, and have explicitly displayed its effect on the accuracy of the solution. Such considerations

may guide the choice of the semi-implicit operator for both MHD and other physical models. We have given both formal and heuristic discussion of the remarkable stabilizing properties of the method.

We have displayed two particular forms of the semi-implicit operator for the MHD equations, and have compared and contrasted their effect on known solutions by performing both linear and nonlinear three-dimensional computations. In the linear phase, we have found that the inclusion of anisotropy in the semi-implicit operator allows accurate computations to be performed with time steps approximately twice as large as required by an extremely simple isotropic operator. In the far nonlinear phase both isotropic and anisotropic forms yield the same physical phenomena, the primary difference being that the relevant frequencies are decreased by approximately 30% when the isotropic form is employed. Each of the semi-implicit computations on the resistive diffusion time scale at $S = 10^3$ required approximately 2 hours of CPU time on a CRAY-I computer. We estimate that the same computations would require over 100 CPU h if each were performed explicitly.

Finally, we have shown that the nonlinear advective term $\mathbf{V} \cdot \nabla \mathbf{V}$ is required to simulate the details of the nonlinear physics. However, global effects can be reproduced if this term is deleted from the model.

We conclude that the semi-implicit method is a simple, fast, and accurate algorithm for three-dimensional MHD simulations. It is simple because it is extremely easy to implement, even in existing codes. (This is especially true in the case of the isotropic operator.) It is fast because the computation time per time step is dominated by the evaluation of nonlinear convolutions. Since (for the case of doubly periodic system) the semi-implicit method requires only the solution of linear tridiagonal systems, it requires essentially the same CPU time per time step as explicit methods, while allowing time steps that may be orders of magnitude larger. It is accurate because the semi-implicit operator can be chosen to mimic the MHD operator for modes of interest. However, a simple isotropic operator yields long-time-scale results that are surprisingly good, and is extremely easy to implement. The ability to simulate driven systems for times that are significant fractions of the resistive diffusion time has led to an identification of previously unknown nonlinear behavior.

APPENDIX

In this Appendix we explicitly display the form of the anisotropic semi-implicit operator, based on Eq. (24), used in this work

$$(\mathbf{G} \cdot \mathbf{V})_r = (C_\theta^2 + C_z^2) \frac{1}{r} \frac{\partial}{\partial r} \left(r \frac{\partial V_r}{\partial r} \right) - \left[\frac{m^2 C_\theta^2 + C_z^2}{r^2} + C_z^2 k^2 \right] V_r$$

$$+ \frac{2imC_z^2}{r^2} V_\theta - \frac{imC_z^2}{r^2} \frac{\partial}{\partial r} (rV_\theta), \tag{A1}$$

$$(\mathbf{G}\cdot\mathbf{V})_\theta = C_r^2 \frac{1}{r}\frac{\partial}{\partial r}\left(r\frac{\partial V_\theta}{\partial r}\right) - \left[\frac{m^2(C_r^2+C_z^2)}{r^2} + C_z^2 k^2\right] V_\theta$$
$$- \frac{imC_z^2}{r^2}\frac{\partial}{\partial r}(rV_r), \tag{A2}$$

$$(\mathbf{G}\cdot\mathbf{V})_z = C_\theta^2 \frac{1}{r}\frac{\partial}{\partial r}\left(r\frac{\partial V_z}{\partial r}\right) - \left[\frac{m^2 C_\theta^2 + C_r^2}{r^2} + (C_r^2+C_z^2)k^2\right] V_z \tag{A3}$$

where C_r^2, C_θ^2, and C_z^2 are determined by Eq. (25).

ACKNOWLEDGMENTS

The authors wish to thank Dr. A. A. Mirin for helpful discussions and for a thorough and critical reading of the manuscript. This work was performed at Science Applications International Corporation under contract DE-AC03-83ER53150/5 with the U.S. Department of Energy, at New York University under contract DE-AC02-76ER03077 with the U.S. Department of Energy, and at Los Alamos National Laboratory under the auspices of the U.S. Department of Energy.

REFERENCES

1. H. R. HICKS, B. CARRERAS, J. A. HOLMES, D. K. LEE, AND B. V. WADDELL, *J. Comput. Phys.* **44**, 46 (1981).
2. E. J. CARAMANA, R. A. NEBEL, AND D. D. SCHNACK, *Phys. Fluids* **26**, 1305 (1983).
3. D. D. SCHNACK, E. J. CARAMANA, AND R. A. NEBEL, *Phys. Fluids* **28**, 321 (1985).
4. M. K. BEVIR AND J. W. GRAY, Proceedings of the Reversed Field Pinch Theory Workshop, Los Alamos National Laboratory Report No. LA-8944-C, (LANL, Los Alamos, 1981), p. 176.
5. B. V. WADDELL, B. CARRERAS, H. R. HICKS, AND J. A. HOLMES, *Phys. Fluids* **22**, 896 (1979).
6. G. VAN HOVEN *et al.*, in *Solar Flares*, edited by P. A. Sturrock (Colorado Associated Press, 1980) p. 177.
7. C. H. FINAN III AND J. KILLEEN, *Comput. Phys. Comm.* **24**, 441 (1981).
8. H. R. STRAUSS, *Phys. Fluids* **20**, 1354 (1977).
9. A. Y. AYDEMIR, D. C. BARNES, E. J. CARAMANA, A. A. MIRIN, R. A. NEBEL, D. D. SCHNACK, AND A. G. SGRO, *Phys. Fluids* **28**, 898 (1985).
10. A. Y. AYDEMIR AND D. C. BARNES, *J. Comput. Phys.* **59**, 108 (1985).
11. A. J. ROBERT, in Proceedings of WMO/IUGG Symposium on Numerical Weather Prediction, Tokyo, 1969.
12. D. S. HARNED AND W. KERNER, *J. Comput. Phys.* **60**, 62 (1985).
13. D. S. HARNED AND D. D. SCHNACK, *J. Comput. Phys.* **65**, 57 (1986).
14. J. B. TAYLOR, *Phys. Rev. Lett.* **33**, 139 (1974).
15. D. G. FOX AND S. A. ORSZAG, *J. Comput. Phys.* **11**, 612 (1973).
16. D. GOTTLIEB AND S. A. ORSZAG, *Numerical Analysis of Spectral Methods* (SIAM, Philadelphia, 1977).
17. D. D. SCHNACK, D. C. BAXTER, AND E. J. CARAMANA, *J. Comput. Phys.* **55**, 485 (1984).
18. F. H. HARLOW AND A. A. AMSDEN, *J. Comput. Phys.* **8**, 197 (1971).
19. S. C. JARDIN AND W. PARK, *Phys. Fluids* **24**, 679 (1981).
20. D. SCHNACK AND J. KILLEEN, *J. Comput. Phys.* **35**, 110 (1980).
21. A. A. MIRIN, R. J. BONUGLI, N. J. O'NEIL, AND J. KILLEEN, *Comput. Phys. Comm.* **41**, 85 (1986).